RESEARCH

Characterization of CCTRC Waveguide and Measurement of Vitamin C Concentration

Zhongbo Wu[1] · Jun Zhu[1,2]

Abstract

In order to realize optical sensing with high sensitivity and the figure of merit, in this study, we propose a metal–insulator-metal (MIM) waveguide structure based on the transmission properties of surface plasmon excitations (SPPs). This structure consists of main waveguide with a metal baffle (MWMB) combined with a copper coin-type ring cavity (CCTRC) and a double semi-elliptical ring cavity (DSERC). We study the electromagnetic characteristics, transmission performance, and sensing performance of the structure by simulating numerical calculations using the finite element method. In addition, we optimize the structural parameters. The results indicate that when the transverse magnetic (TM) wave is incident on the main waveguide, the designed MIM waveguide structure exhibits double Fano resonance peaks at incident wavelengths at 842 nm and 926 nm, with total electric field energies of 2.93×10^{-14} J and 2.35×10^{-14} J, respectively. At the same wavelengths, total magnetic field energies are 1.33×10^{-14} J and 1.32×10^{-14} J, respectively. Therefore, the proposed structure can be used for the refractive index sensor. The extant structure's sensitivity and the figure of merit are 1150 nm/RIU and 115, respectively. The resonance wavelength shift was identified, allowing the present structure to measure the concentration of aqueous vitamin C solutions.

Keywords Sensors · MIM · Waveguide · Fano resonance

Introduction

Surface plasmon polaritons (SPPs) are electromagnetic modes generated by the interaction between light waves and migratory charges on metal surfaces, which decay exponentially in the direction of intensity perpendicular to the intersection [1]. Traditional optical devices are limited by the optical diffraction limit; the minimum size of the photonic device can only be limited to about half of the wavelength of the light; when the photonic device is reduced to a certain degree, the loss of the device increases, which seriously affects the performance of the device. It is difficult to achieve a high degree of integration of photonic devices. It is a unique surface electromagnetic wave that propagates along the surface of a conductor in the optical frequency range. SPPs have properties such as strong optical confinement in the subwavelength range and local field enhancement effects. Moreover, it is able to break the optical diffraction limit [2]. Thus, SPPs can produce special optical properties at the nanoscale. Thus, it is of great significance in the future development of photonic devices.

As opposed to conventional Lorentzian spectral lines, Fano resonance spectral lines exhibit significantly sharp and asymmetric line shapes, which means that a small change in the structure causes a sharp change in the resonance characteristics of the Fano line shape. This allows for high sensitivity sensing and is made possible by the narrower line width of Fano resonance spectral lines. Due to the reduced line width of Fano resonance, Fano resonance possesses narrower full width at half maximum (FWHM) and higher figure of merit (FOM) [3].

Many existing new optical devices can realize nanoscale integration, and waveguide structures such as metal nanoparticle arrays, hybrid Bragg waveguides, metal nanowires,

✉ Jun Zhu
zhujun1985@gxnu.edu.cn

1   College of Electronic Engineering, Guangxi Normal University, Guilin 541004, China

2   Key Laboratory of Space Photoelectric Detection and Perception, Ministry of Industry and Information Technology, Nanjing University of Aeronautics and Astronautics), No. 29 Yudao Street, Nanjing 210016, China

and V-slot waveguides have also been proposed by researchers, but they are in comparison with the MIM waveguide; the electromagnetic wave in the propagation of the resulting loss is greater, the limit distance of propagation is shorter, and the degree of integration is lower. metal–insulator-metal (MIM) waveguide structures based on SPPs have the advantages of high confinement, low loss degree, low bending loss, and a relatively simple preparation process. It has been widely used in a variety of optical devices, including sensors [4, 5], filters [6], optical switches [7, 8], and splitters [9]. Fano resonance based on SPPs with MIM waveguide excitation has great research prospects in the field of refractive index sensing. For example, Zhao et al. designed a plasmonic waveguide coupling system with a MIM waveguide, two silver baffles, and a coupling ring cavity [10]. This achieved a maximum sensitivity of 718 nm/RIU and a figure of merit of 4354, which provided guidance for the design of SPP-based guidance for design of high-sensitivity on-chip sensors. Yang et al. proposed a MIM waveguide structure consisting of a cross-shaped cavity and a baffle with a linear refractive index sensitivity of 1100 nm/RIU and a figure of merit about 1.08×10^5. The established structure has a large potential for applications in nanosensors and spectral splitters [11]. Tang et al. proposed a structure of MIM waveguides coupled with ring and rectangular resonators for plasmonic refractive index sensors with a sensitivity of up to 1125 nm/RIU [12].

In this paper, we propose a MIM waveguide structure, which consists of a main waveguide with a metal baffle coupled with copper coin-type ring cavity (CCTRC) and double semi-elliptical ring cavity (DSERC). It can generate double Fano resonance. Double Fano resonance at the same time in the sensing can form differential sensing, through the idea of differential sensing can effectively solve the measurement error caused by external factors. We analyze the structure by the finite element method (FEM). Furthermore, we study the influence of the structural parameters of the coupling system on the Fano resonance and the electric field distribution, transmission performance, and sensing performance of the structure and we improve those parameters. The results show that the structure can generate double Fano resonance and can achieve sensing by resonance wavelength shift, the sensitivity of the structure is 1150.00 nm/RIU, and the FOM is 115. We use the structure to achieve the function of measuring the concentration of vitamin C aqueous solution.

Structural Model and Analysis Methods

The MIM waveguide structure proposed in this paper consists of a main waveguide with a metal baffle main waveguide (MWMB) coupled with a copper coin-type ring cavity (CCTRC) and a double semi-elliptical ring cavity (DSERC) for the preparation of a plasmonic refractive index sensor.

Figure 1 shows a two-dimensional cross-sectional schematic of the present waveguide structure.

The power of the input port is $P_{in} = 1$ W. The photons and electrons oscillate collectively, resulting in swift waves that excite SPPs on the dielectric and metal surfaces [13, 14]. We chose silver as the metal dielectric and used air as

Fig. 1 Two-dimensional cross-sectional view of MIM waveguide structure
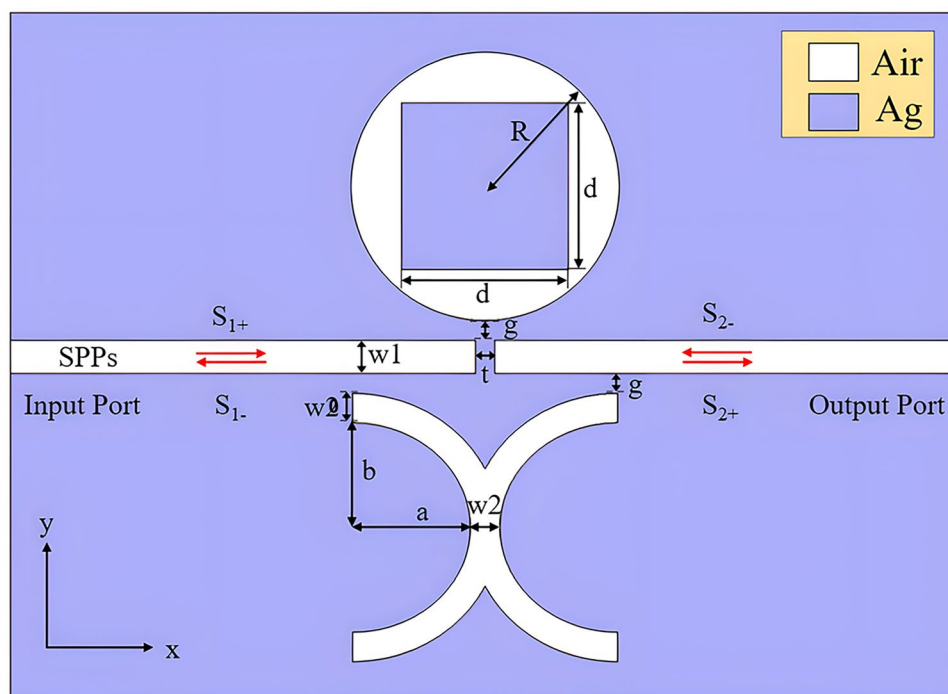
the insulator-filling material for the model simulation. The width of the main waveguide in the figure is w1.To ensure that only the transverse magnetic wave (TM) propagates in the straight waveguide, the width of the main waveguide is constant at w1 = 50 nm [15]. The metal baffle is placed in the middle of the main waveguide with a width of *t*. The coupling width of both CCTRC and DSERC to the main waveguide is *g*. *R* is the outer diameter of CCTRC. *d* is the side length of the nanosilver square inside CCTRC. DSERC consists of two semi-elliptical ring cavities of identical dimensions. w2 is the width of the semi-elliptical ring cavity. *a* and *b* are the long and short axis lengths of the elliptical inner ring cavity, respectively. The light is incident from the left side of the MIM waveguide and exits from the right side of the MIM waveguide. S1 + and S1 − are the amplitudes of the incident light and the outgoing light at the input, respectively; S2 + and S2 − are the amplitudes of the incident light and the outgoing light at the output, respectively. The transmittance (*T*) at the output port is the ratio of the output power (P_{out}) to the input power (P_{in}), $P_{in} = \int Poavx dS$, $P = \int Poavx dS2$, Poavx is the component of the time-averaged power flow in the axial direction and the cross-sectional areas of P_{in} and P_{out}, respectively [16].

Ugo Fano obtained the expression for the Fano resonance line spectrum by the superposition principle of quantum mechanics, which is the Beutler-Fano formula [17]:

$$\sigma = \frac{(\varepsilon + q)^2}{\varepsilon^2 + 1} \tag{1}$$

where *q* describes the degree of asymmetry of the line shape and is called the Fano shape parameter. *ε* denotes the approximate energy, defined as $2(E - E_F)\Gamma$. E_F is a resonance energy that indicates the position of the Fano resonance peak. *Γ* is the linewidth of the self-ionized state. The asymmetry parameter *q* is the ratio that represents the probability of jumping to the mixed and continuous states. When *q* = 0, the resonance spectral line behaves as an anti-resonance form. When *q* = 1, the overall energy jumps to the discrete and continuous states with the same intensity, and an asymmetric Fano line shape appears. When *q* = ±∞, the overall energy exhibits a transition to the discrete state, and a symmetric Lorentzian line shape forms.

The relative permittivity of air is 1.0. The relative permittivity of silver can be determined by the Drude model [18–20]:

$$\varepsilon_m = \varepsilon_\infty - \frac{\omega_p^2}{\omega^2 - i\omega\gamma} \tag{2}$$

ω is the angular frequency of the incident wave, the permittivity $\varepsilon_\infty = 3.7$ at infinite angular frequency, and $\omega_p = 9.1$ (eV) is the plasma frequency. $\gamma = 0.018$ is the electron collision frequency. In TM mode, the dispersion relations of

surface plasmon polaritons (SPPs) in the MIM waveguide structure are as follows [21]:

$$\tan h \left(\frac{d\sqrt{\beta^2 - k_0^2 \varepsilon_{in}}}{2} \right) = \frac{-\varepsilon_{in}\sqrt{\beta^2 - k_0^2 \varepsilon_{in} \varepsilon_m(\omega)}}{\varepsilon_m(\omega)\sqrt{\beta^2 - k_0^2 \varepsilon_{in}}} \tag{3}$$

where ε_{in} and $\varepsilon_m(\omega)$ are the dielectric constants of the insulator and metal, respectively. *β* is the propagation constant of the SPPs, and k_0 is the vacuum wave vector, denoted as [22]

$$k_0 = \frac{2\pi}{\lambda} \tag{4}$$

We use standing wave theory to represent the resonant wavelength [23, 24]:

$$\lambda = \frac{2Re(n_{eff})L_{eff}}{m - \psi/\pi}, (m = 0, 1, 3...) \tag{5}$$

where Re(*n*eff) is the real part of the effective refractive index of the fiber, *L*eff is the effective length of the resonant cavity, *m* is the order of the SPPs resonance, and *ψ* is the reflected phase shift of the SPPs in the resonant cavity. The SPPs in the resonant cavity and the SPPs in the main waveguide are superimposed and coupled to each other to show the Fano resonance in the spectrum.

Simulation Analysis and Result Analysis

Structure Construction

The transmission spectrum and electromagnetic field distribution are calculated by the FEM in this structure, and a perfectly matched layer (PML) is designed as a boundary condition. We place a metal baffle in the main waveguide, which allows the incident light to be reflected multiple times in the waveguide, and the amplitude and phase of the light waves are shifted. In this structure, we can change the transmission spectrum of the structure by adjusting it to produce the Fano resonance.

For researching the sensing performance of the structure, we set initial values for the geometric parameters of the structure: first, we used air as a medium in the insulating layer, which has a refractive index of 1, w1 = 50 nm, *t* = 10 nm, *g* = 10 nm, *R* = 210 nm, *d* = 255 nm, w2 = 40 nm, *a* = 180 nm, *b* =160 nm. Figure 2a shows that the structure produces a broadband continuum state when there is only the MWMB in the structure. The transmission spectrum has a relatively stable transmittance and produces two Lorentz peaks at 664 nm and 962 nm. After coupling DSERC directly below the main waveguide only, the structure produces a narrow-band discrete state and interferes with the
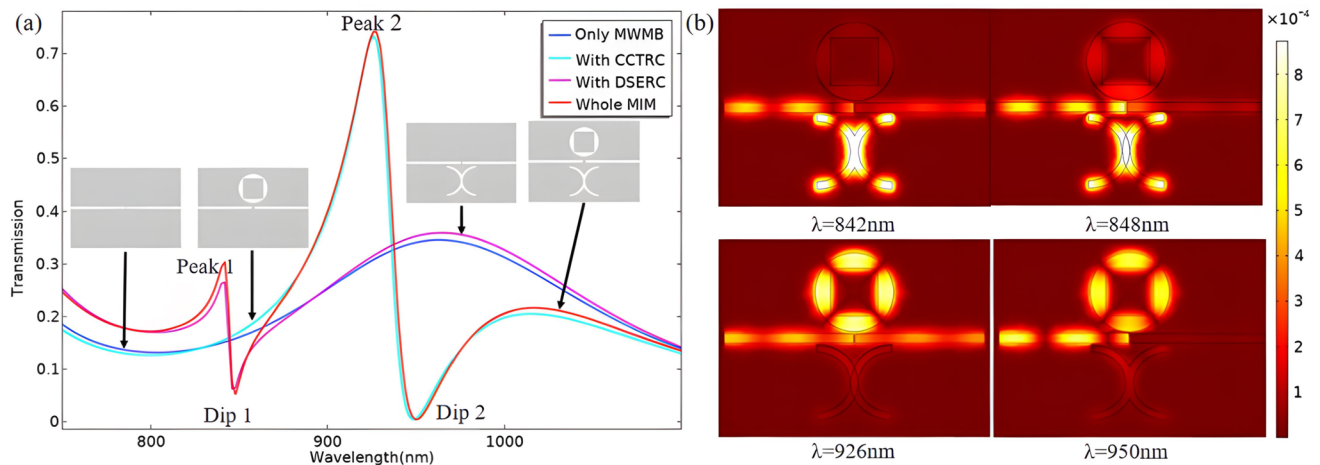
Fig. 2 Transmission spectra of the structure combinations and their corresponding magnetic field distributions: **a** transmission spectra of MWMB only (blue line), with CCTRC (cyan line), with DSERC (violet line), and the whole MIM waveguide structure (red line). **b** Magnetic field distributions of the MIM waveguide at wavelengths of $\lambda = 842$ nm, $\lambda = 848$ nm, $\lambda = 926$ nm, and $\lambda = 950$ nm, respectively

broadband continuum to produce the first Fano resonance (FR1). After coupling CCTRC directly above the main waveguide only, the structure produces a narrow-band discrete state and interferes with the broadband continuum to produce the second Fano resonance (FR2). In the complete MIM structure, the above two Fano produced two resonance peaks, Peak1 and Peak2, at $\lambda = 842$ nm and $\lambda = 926$ nm, respectively, and two resonance troughs, Dip1 and Dip2, at $\lambda = 848$ nm and $\lambda = 950$ nm. From Fig. 2b, we can observe that the magnetic fields of Peak1 and Dip1 are mainly concentrated at DSERC, which means that we change the energy distribution by changing the structural parameters of DSERC to achieve the tuning of FR1. The magnetic fields of Peak2 and Dip2 are mainly concentrated at CCTRC, which means that we change the energy distribution by changing the structural parameters of CCTRC to achieve the tuning of FR2 by changing the structural parameters of CCTRC to change the energy distribution to achieve the tuning of FR2. In addition, we can also change the transmission spectrum of the broadband continuum by changing the baffle thickness t or change the coupling state by changing the coupling distance g to tune the transmission spectrum.

We also discuss the variation of the total electric field energy and the total magnetic field energy of the MIM structure at different wavelengths, as shown in Fig. 3. When a metal baffle is added to the main waveguide, the SPPs do not propagate directly along the waveguide and are partially reflected at the baffle. Other reflected energy enters into the CCTRC and DSERC, and the other energy interferes with the SPPs traveling forward along the waveguide, which leads to a sharp change in phase at 843 nm and 928 nm. Due to the significant perturbation of the phase in the waveguide, asymmetric Fano resonance lines appear in the

transmission spectrum and the energy capacity aggregates. We can observe that two sharp Lorentzian peaks can be seen at 843 nm and 928 nm. The first wave crest corresponds to total electric field energy of 2.93×10^{-14} J and FWHW of 7. It has a total magnetic field energy of 1.33×10^{-14} J and FWHM of 7. The second wave crest corresponds to a total electric field energy of 2.35×10^{-14} and FWHW of 19; it has a total magnetic field energy of 1.32×10^{-14} J and FWHM of 19. Compared with the total energy of the magnetic field, the total energy of the electric field is significantly higher. However, the corresponding FWHM is almost unchanged because the structure loses some energy due to thermo-optical effects when the electric field is converted to a magnetic field [25, 26]. The energy lost is relatively uniform at all wavelengths so that the present structure can still enable SPPs, resulting in strong resonance interference and Lorentzian resonance, which would make the FWHM particularly small [27, 28].

Structural Parameter Analysis and Performance Analysis

After determining the post-section model, we analyze and optimize the MWMB, CCTRC, and DSERC structural parameters by controlling variables for both transmittance and FWHM, respectively. FWHM is the full width at half maximum and is related to the sensor resolution and FOM.

For MWMB, we discuss the relationship between the transmission spectra and the variation of the FWHM and transmittance of the Fano resonance with the baffle thickness t increases from 10 to 25 nm in steps of 5 nm, as shown in Fig. 4a. Figure 4b shows that as t increases, the FWHM change of Peak1 tends to be smooth and floats between 6

Fig. 3 Total energy of electric field and total energy of magnetic field at different wavelengths
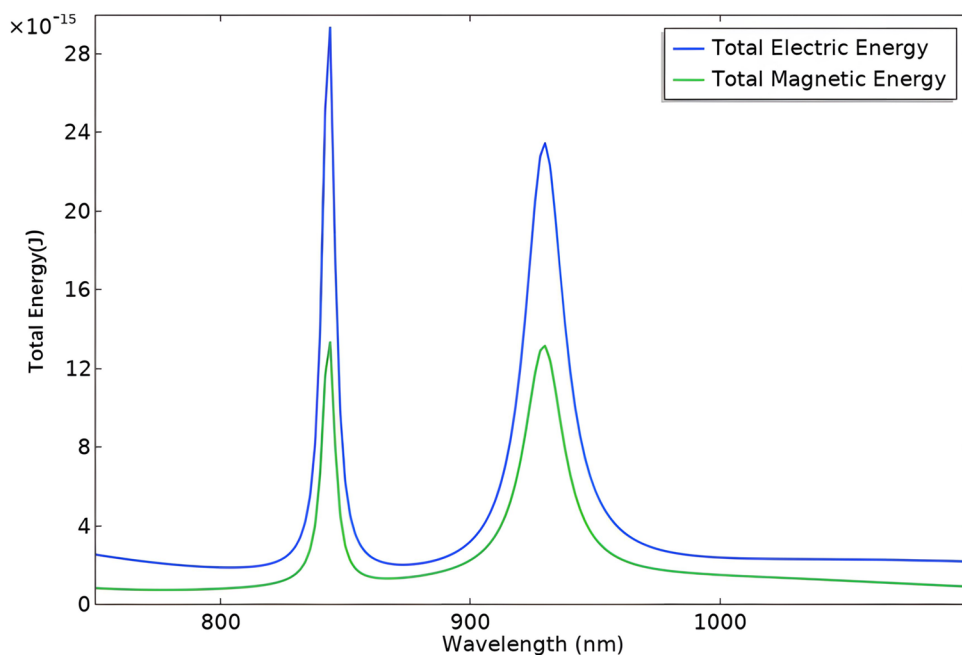
and 9 nm. The FWHM of Peak2 decreases from 26 to 19 nm. However, the FWHM of Dip1 and Dip2 gradually increases from 5 to 28 nm and from 18 to 30 nm gradually disappears, respectively. As t increases, the transmittance of Peak1 and Peak2 decreases. The transmittance of Peak1 decreases from 0.43 to 0.16 with an extreme difference of 0.27. The transmittance of Peak2 decreases from 0.79 to 0.60. Metal baffles are used to form a wider continuum as the TM wave enters the waveguide structure. Compared to in a dielectric, the transmission of light to metal is poor, and as the thickness of the metal–metal baffle increases, the transmittance of the device decreases significantly, which affects the output characteristics of the device. With comprehensive reference to the preparation process and the variation of FWHM and transmittance, we choose the baffle thickness as $t = 10$ nm.

Then we discuss the transmission spectra of MWMB coupling distance g with CCTRC and DSERC in steps of 5 nm from 5 to 20 nm and the relationship between FWHM and
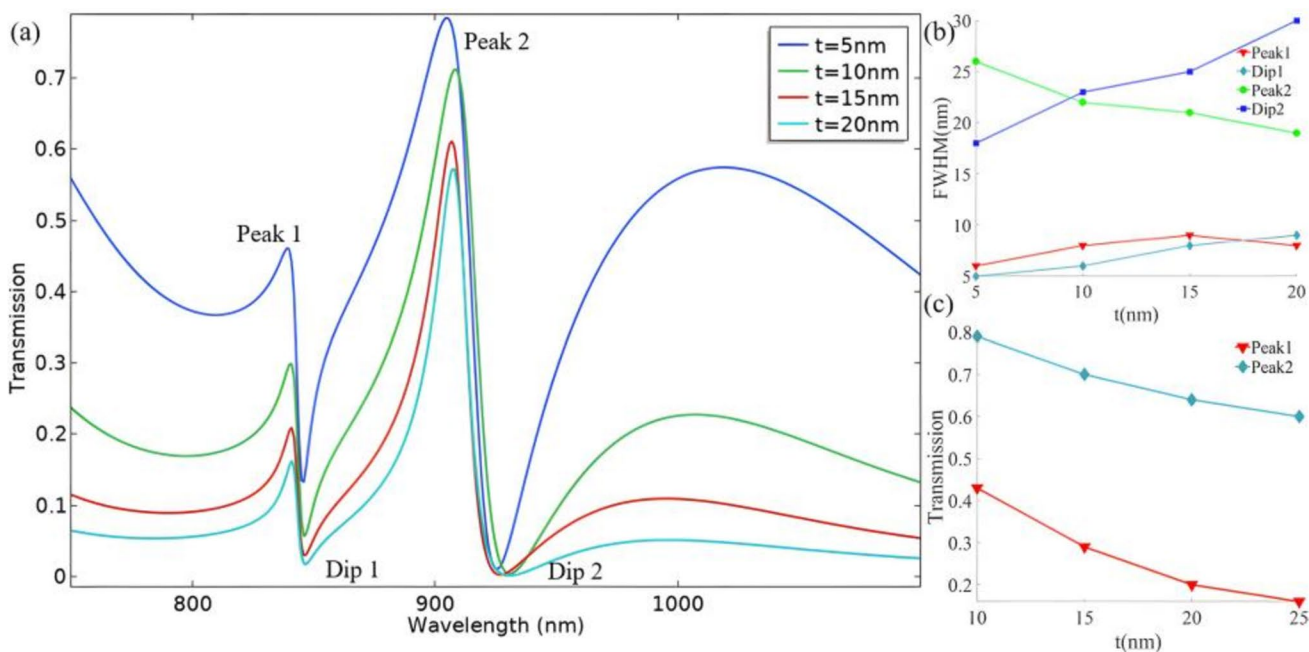

Fig. 4 a Transmission spectra of t increasing from 5 to 25 nm. **b**, **c** FWHM and transmittance of Fano resonance spectral line with the value of t

transmittance of Fano resonance, as shown in Fig. 5a. With the increase of g, Peak1 appears significantly blue shifted. This means the FR2 resonance wavelength position can be tuned by adjusting g. Figure 5b shows that the FWHM all decreases significantly as g increases. The FWHM of Peak1 decreases from 14 to 7 nm, the FWHM of Dip1 increases from 13 to 6 nm and then to 9 to 7 nm, the FWHM of Peak2 decreases from 28 to 18 nm, and the FWHM of Dip2 decreases from 34 to 14 nm. Figure 5c shows that as g increases, the transmittance of Peak1 and Peak2 appears to decrease significantly, from 0.43 to 0.17 with a polar difference of 0.26 and from 0.8 to 0.53 with a polar difference of 0.27, respectively. The larger the coupling spacing is, the more difficult it is for the SPPs in the waveguide to couple into the resonator, and the weakening of the resonance leads to the reduction of the transmittance; that is, there is a negative correlation between the coupling spacing and the transmittance. With comprehensive reference to the complexity of the preparation process and its FWHM and transmittance variation, we choose the coupling distance as $g = 10$ nm.

For CCTRC, we perform parametric analysis and optimization of the outer diameter R. We analyze the transmittance spectra and the changes of FWHM and transmittance of Fano resonance when R increase from 200 to 215 nm in steps of 5 nm. As shown in Fig. 6a, with the increase of R, the position of FR1 corresponds to the wavelength into a very small blue shift, and the amplitude gradually decreases. The interference phenomenon gradually diminishes, and FR2 shows a significant redshift. This means that we can independently tune the FR2 resonance wavelength position by adjusting the length of R. Figure 6(b shows that as R increases, the

FWHM of Peak1 decreases from 9 to 8 nm, the FWHM of Dip1 decreases from 17 to 7 nm and stabilizes, the FWHM of Peak2 shrinks from 37 to 12 nm, but the FWHM of Dip2 gradually increases from 17 to 25 nm. With comprehensive reference to the changes in FWHM and transmittance, we choose the outer diameter of CCTRC as $R = 215$ nm.

For DSERC, we analyze and optimize the cavity width w2 and the long axis a and short axis b of the inner cavity of the semi-elliptic ring.

Firstly, we analyze the transmission spectrum and the relationship between the FWHM and transmittance of the Fano resonance for MWMB with increases in the baffle thickness t from 10 to 25 nm in steps of 5 nm. As shown in Fig. 7a, when w2 = 35 nm, the amplitude of FR1 transmission spectrum is very small. The interference is not apparent, which is not adopted. As w2 increases, the FR1 resonance wavelength is significantly blue shifted, the amplitude gradually increases, and FR2 shows a very slight blue shift. This means we can independently tune the resonance wavelength position of FR1 by adjusting the length of w2. Figure 7b shows that between w2 = 40 nm and w2 = 50 nm, the FWHM of Peak1 gradually decreases from 8 to 6 nm as w2 increases, the FWHM of Dip1 first increases from 7 to 11 nm and then decreases to 9 nm, the FWHM of Peak2 increases from 10 to 28 nm, and the FWHM of Dip2 remains unchanged at 25 nm. The transmittance of FR1 varies slightly from 0.3 to 0.38 from w2 = 40 nm to w2 = 50 nm, and the transmittance of FR2 decreases slightly from 0.72 to 0.70. With comprehensive reference to the FWHM and the variation of transmittance, we choose the ring cavity width of DSERC as w2 = 40 nm.
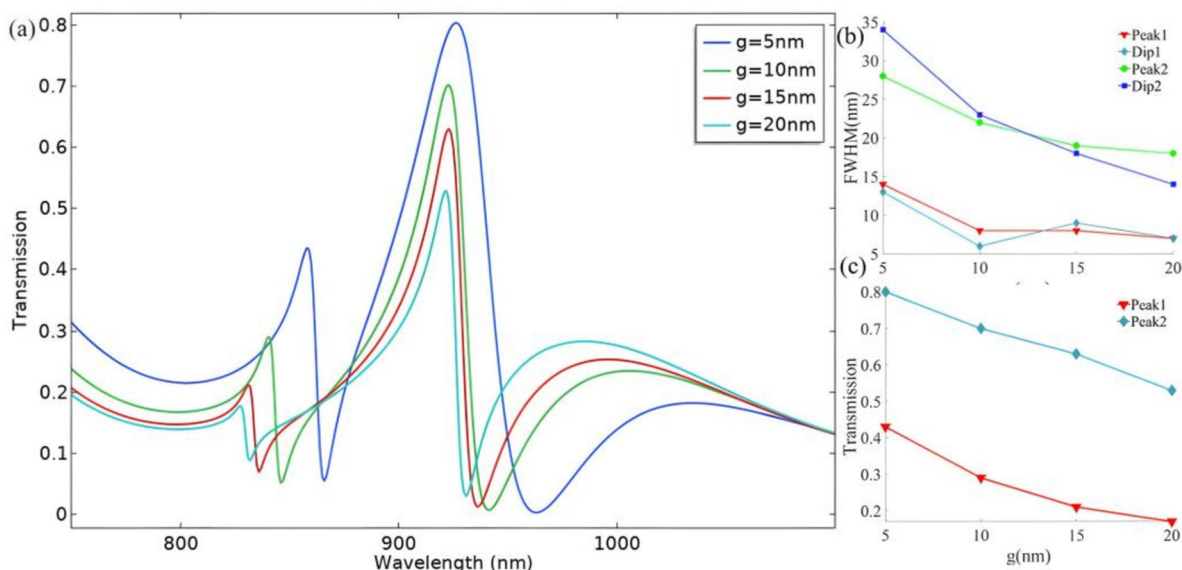

Fig. 5 **a** Transmission spectra of g increasing from 5 to 20 nm. **b**, **c** FWHM and transmittance of Fano resonance spectral lines with respect to the value of g
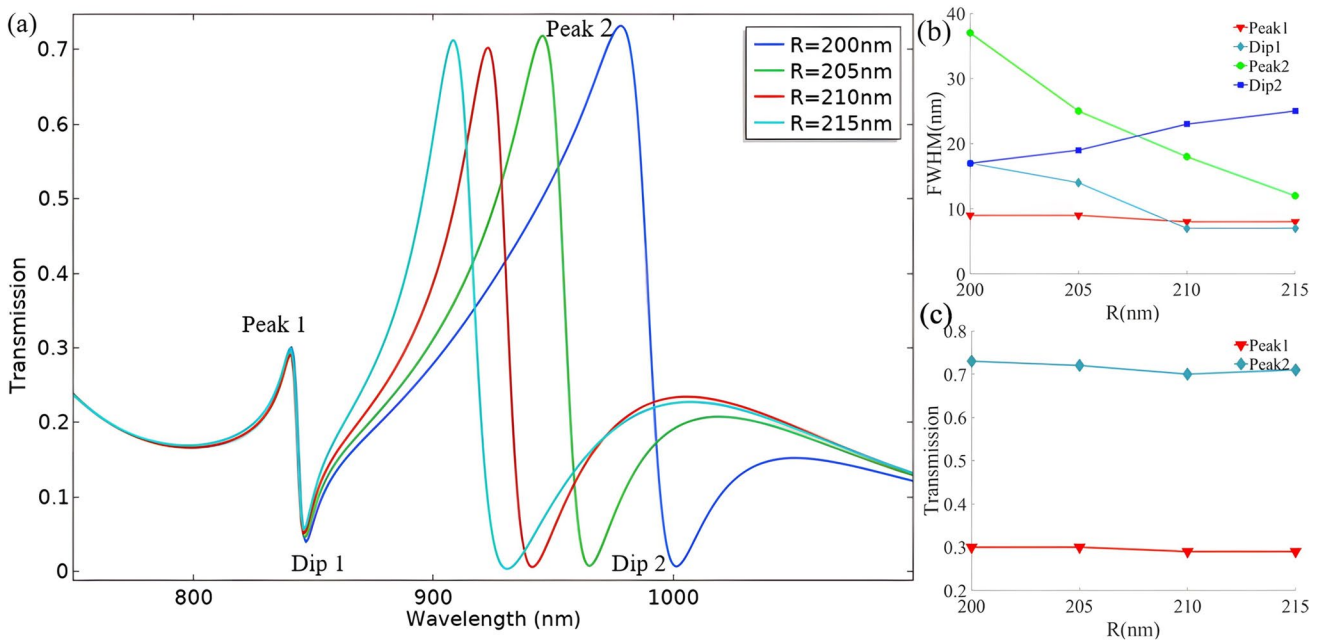
Fig. 6 **a** Transmission spectra of R increasing from 200 to 215 nm. **b**, **c** FWHM and transmittance of Fano resonance spectral lines as a function of *R* value

Then, we analyze the transmission spectra of the elliptical ring inner cavity with the long axis *a* increasing from 175 to 190 nm in steps of 5 nm and the relationship between the FWHM and the transmittance of the Fano resonance. As shown in Fig. 8a, FR1 shows a significant red shift and a significant increase in amplitude, and the transmission spectrum of FR2 is almost not shifted. This means that we can independently tune the resonant wavelength position of FR1 by adjusting the length of *a*. Figure 8b shows that as the *a* increases, the FWHM of Peak1 increases significantly from 7
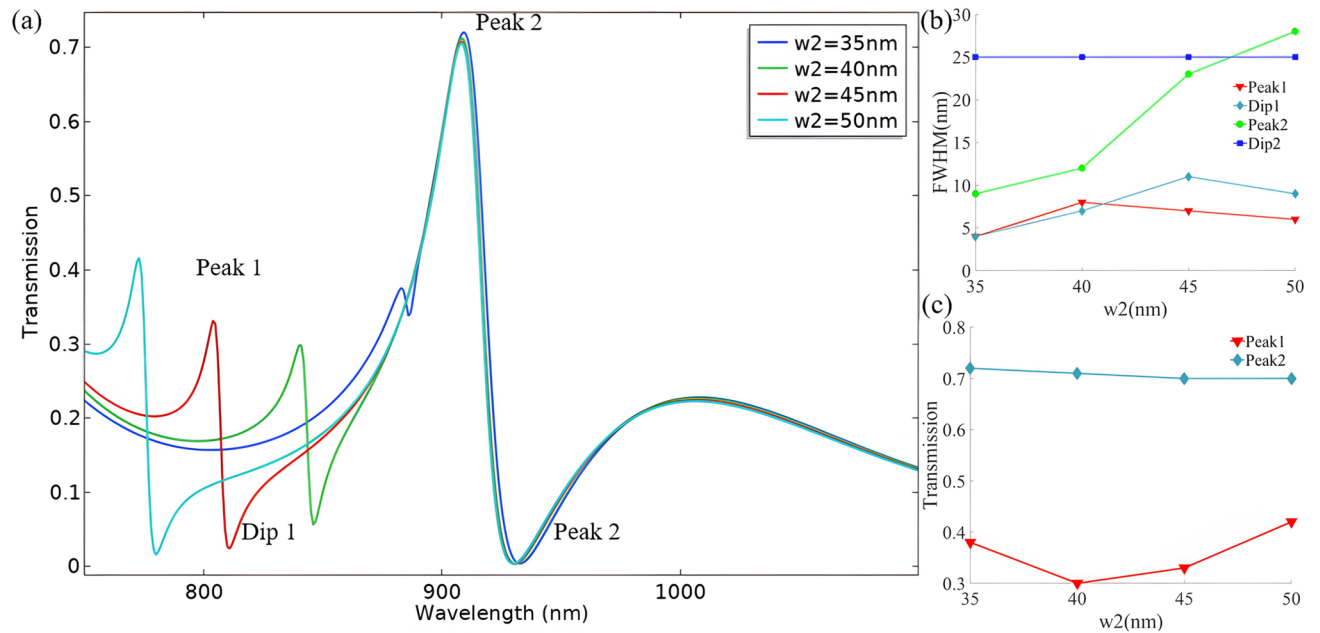

Fig. 7 **a** Transmission spectra of w2 increasing from 35 to 50 nm. **b**, **c** FWHM and transmittance of Fano resonance spectral lines as a function of w2 value
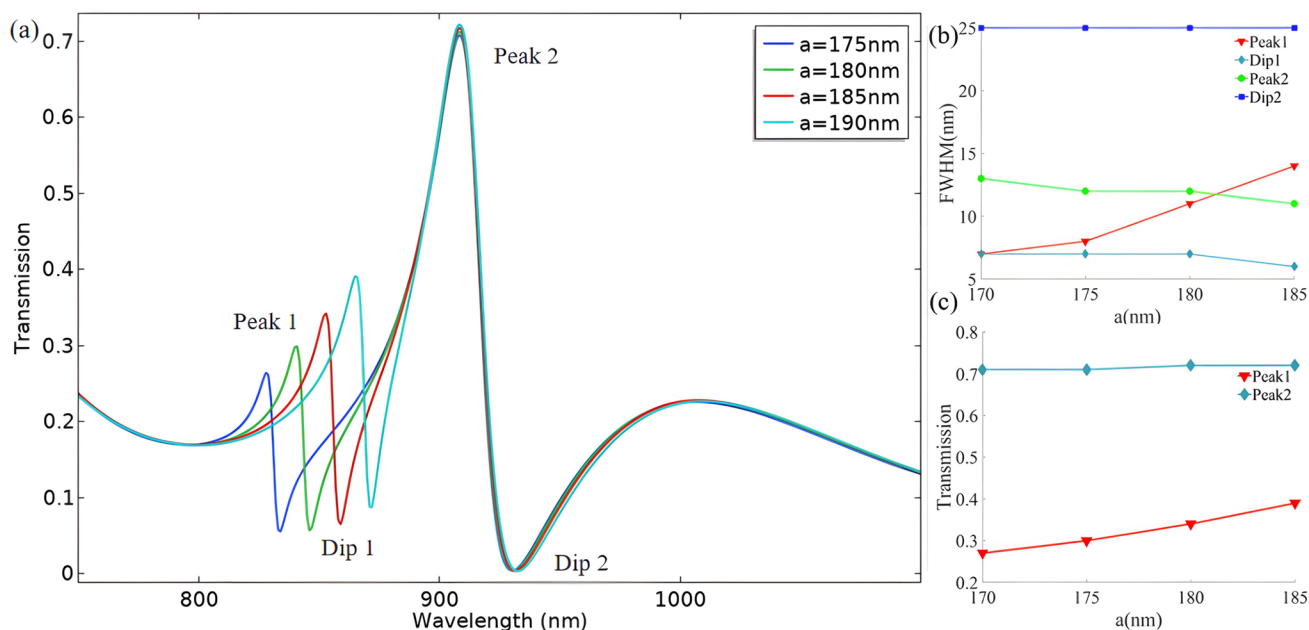
Fig. 8 **a** Transmission spectra of *a* increasing from 175 to 190 nm. **b**, **c** FWHM and transmittance of Fano resonance spectral lines with respect to the value of *a*

to 14 nm, the FWHM of Dip1 decreases slightly from 7 to 6 nm, the FWHM of Peak2 decreases from 13 to 11 nm, and the FWHM of Dip2 remains unchanged at 25 nm. Figure 8c shows that the transmittance of FR1 increases from 0.27 to 0.39, and FR2 increases slightly from 0.71 to 0.72. Referring to the changes of FWHM and transmittance together, we choose the long axis of the inner cavity of the elliptical ring as *a* = 190 nm.

Then, we analyze the transmission spectra of the short axis *b* of the inner cavity of the elliptical ring when increasing from 150 to 165 nm in steps of 5 nm and the relationship between the FWHM and transmittance changes of the Fano resonance. As shown in Fig. 9a, FR1 shows a significant red shift and a significant decrease in amplitude, and the transmission spectrum of FR2 is almost not shifted. This means that we can independently tune the resonance wavelength position of FR1 by adjusting the length of *b*. Figure 9b shows that as *b* increases, the FWHM of Peak1 increases from 13 to 15 nm, the FWHM of Dip1 decreases from 8 to 5 nm, Peak2 decreases slightly from 11 to 10 nm, and Dip2 is constant at 11 and 30 nm. Figure 9c shows that the transmittance of FR1 decreases from 0.41 to 0.39 and then increases to 0.40, and the transmittance of FR2 remains at 0.72. Referring to the variation of FWHM and transmittance together, we choose the short axis of the inner cavity of the elliptical ring as *b* = 165 nm.

The optimized structural parameters are w1 = 40 nm, *t* = 10 nm, *g* = 10 nm, *R* = 215 nm, *d* = 255 nm, w2 = 40 nm, *a* = 190 nm, and *b* = 165 nm. From Table 1, we can see the Fano resonance wavelengths and FWHMs corresponding to Peak1, Dip1, Peak2, and Dip2 after optimization.

Sensing Performance Analysis

After determining the structural parameters, we also introduce sensitivity (*S*) and the figure of merit (FOM) to measure the sensing performance of the structure, and we use sensitivity (*S*) to reflect the sensitivity of the sensor to the refractive index of the medium. It is calculated by the following expression [29]:

$$S = \frac{\Delta\lambda}{\Delta n} \tag{6}$$

$\Delta\lambda$ is the offset of the Fano resonance wavelength, Δn is the change in refractive index, and the unit of *S* is nanometer per refractive index unit [30].

The figure of merit (FOM) is an important indicator of the performance of the refractive index sensor, and a larger value of FOM indicates a better sensing performance of the sensor, which is expressed as [31, 32]

$$FOM = \frac{S}{FWHM} \tag{7}$$

Figure 10a shows the Fano transmission spectrum of the material to be measured when the refractive index *n* is increased from 1.00 to 1.06 in steps of 0.02. It can be seen that the transmission spectrum is redshifted overall with increasing refractive index, where Peak1 is redshifted from 874 to 940 nm, Dip1 is redshifted from 896 to 846 nm, Peak2 is redshifted from 909 to 978 nm, and Dip2 is redshifted from 933 to 1004 nm. Figure 10b shows the variation
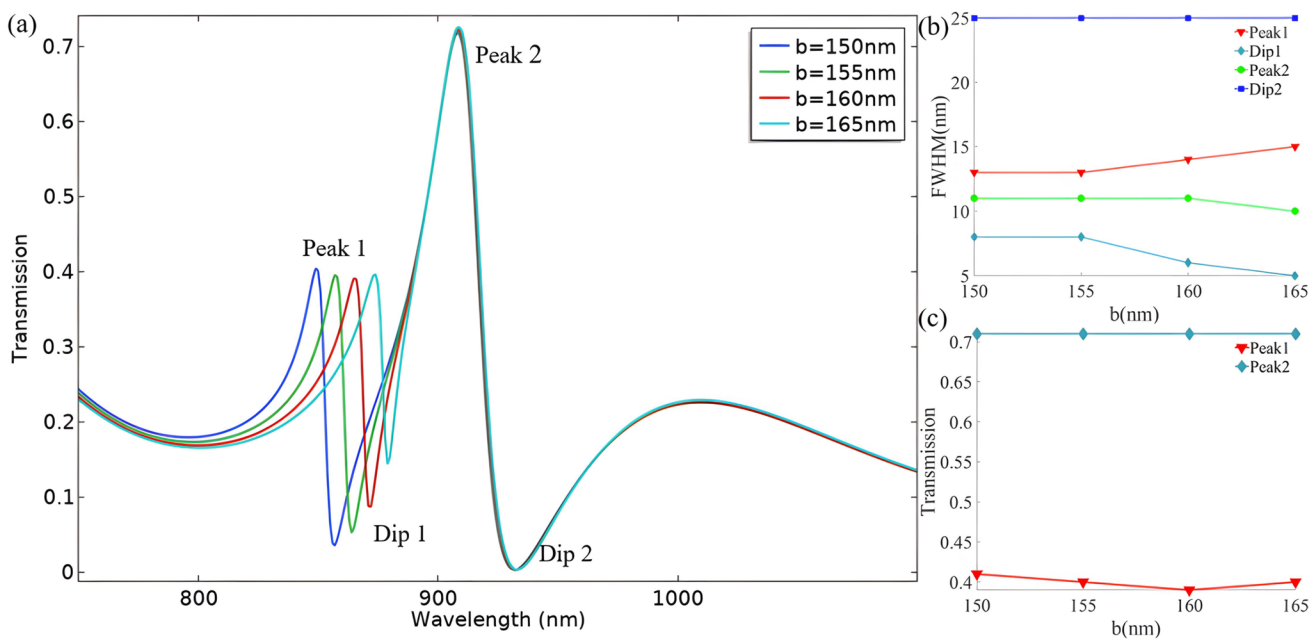
Fig. 9 **a** Transmission spectra of b increasing from 150 to 165 nm. **b**, **c** FWHM and transmittance of Fano resonance spectral lines as a function of *b* value

Table 1 Wavelength λ and FWHM of Fano resonance for the optimized structure

Parameter	FR1		FR2	
	Peak1	Dip1	Peak2	Dip2
λ (nm)	874	879	909	933
FWHM (nm)	15	5	10	25

of Fano resonance wavelength with refractive index *n* for the present structure. We calculated by Eqs. 4 and 5 that the sensitivity of Peak1 is 1100.00 nm/RIU with a FOM of 73.33, Dip1 is 1116.67 nm/RIU with a FOM of 233.33, Peak2 is 1150 nm/RIU with a FOM of 115.00. The results show that the structure has good sensing performance and can achieve the maximum sensitivity of 1183.33 nm/RIU,
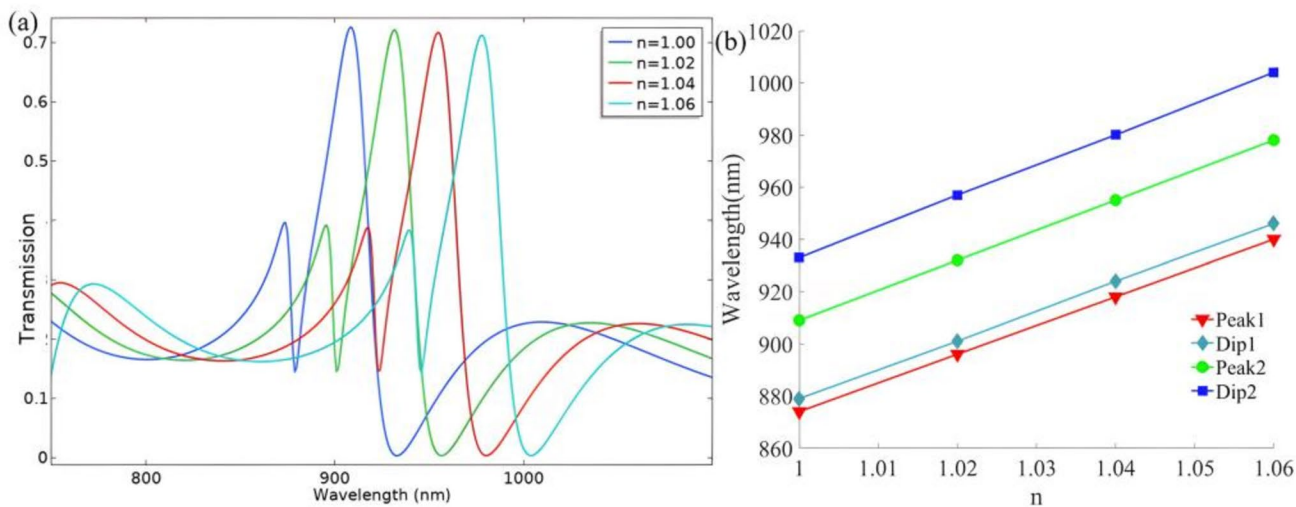

Fig. 10 **a** Transmission spectrum for increasing n from 1.00 to 1.06. **b**, **c** Fano resonance wavelength as a function of *n*

Table 2 Comparison of sensitivity S and FOM of this structure with other sensor structures

References	S (nm/RIU)	FOM
[33]	750	53.7
[34]	540	101
[35]	1160	116
[36]	1153.85	53
This structure	1183.33	115

corresponding to the FOM of 233.33. The comprehensive reference sensitivity and FOM, the final choice of Peak2 to achieve the sensing function, and Peak2 resonance wavelength λPeak2 for linear fitting results are as follows:

$$\lambda_{Peak2} = 1150.00 * n - 241.00 \quad (8)$$

We compare the performance of the designed sensor with other sensors of the same type, and the results are shown in Table 2. The comparison shows that our proposed sensor has higher sensitivity and better FOM values than most of the previously designed sensors.

Based on the sensing characteristics of this structure, we design the sensors to detect the concentration of vitamin C. Vitamin C injection can be used for the treatment of scurvy, as well as for the adjuvant treatment of various acute and chronic infectious diseases and purpura, the treatment of chronic iron poisoning, and also for vitamin C injection to alleviate ovarian cancer treatment [37]. However, excessive intake of vitamin C causes procoagulant and prothrombotic activation of red blood cells and increases thrombosis in vivo [38]. Therefore, the design of a high-precision vitamin C concentration measurement instrument is of great importance in the medical field.

As shown in Fig. 11, we measure the concentrations of five sets of solutions at constant temperature (28.1 °C) using an Abel refractometer [39, 40], and we configure aqueous vitamin C solutions with concentrations of 5%, 10%, 15%, 20%, 25%, and 34% (saturated) from left to right.

Fig. 11 Abel refractometer measurements of aqueous vitamin C solutions at concentrations of 5%, 10%, 15%, 20%, 25%,and 34% (saturated)

The concentration c of aqueous vitamin C solutions at different concentrations versus refractive index are shown in Table 3.

We take the average of the above values and perform a linear fit to obtain the relationship between the fitted vitamin C water concentration c and the n of refractive index as

$$n = 0.13596 * c + 1.33480 \quad c \leq 34\% \quad (9)$$

The linear relationship between the Fano resonance wavelength λ_{Peak2} of Peak2 and the concentration c can be obtained from Eqs. (8) and (9) as

$$\lambda_{Peak2} = 156.354 * c + 1294.020 \quad c \leq 34\% \quad (10)$$

As shown in Fig. 12a, we fill the sensor with 5%, 10%, 15%, 20%, 25%, and 34% aqueous vitamin C. The corresponding wavelength of Fano resonance is red-shifted as the concentration increases. Figure 12b shows the linear fit between the concentration c of the aqueous glucose solution and the refractive index n.

Table 3 Concentration c and refractive index n of aqueous vitamin C solutions at 5%, 10%, 15%, 20%, 25%, and 34% (saturated)

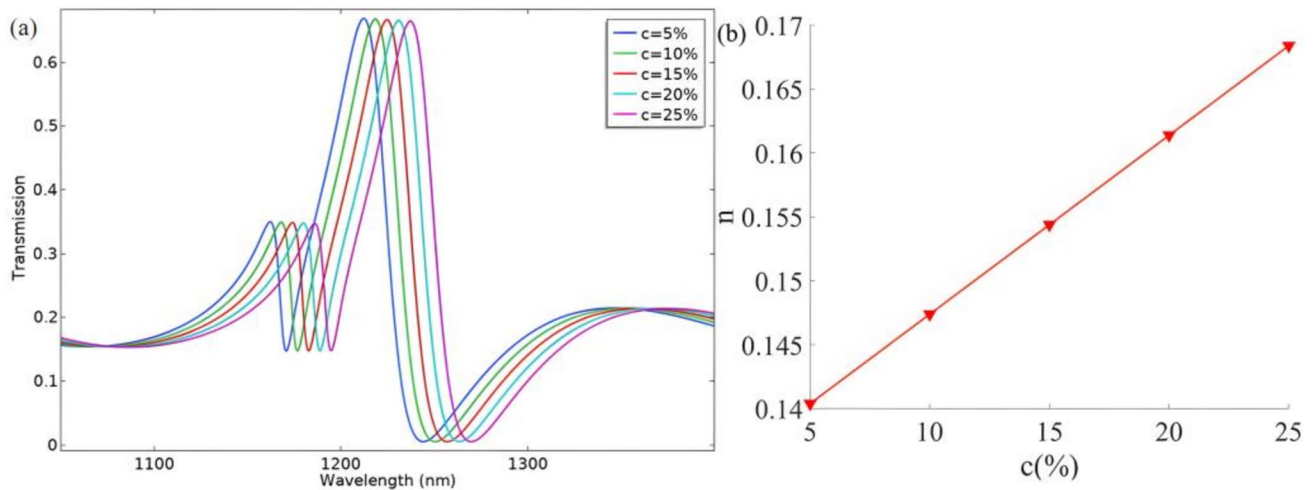| Group	5%	10%	15%	20%	25%	34%
Group 1	1.3415	1.3484	1.3551	1.3619	1.3690	1.3810
Group 2	1.3416	1.3486	1.3552	1.3620	1.3687	1.3808
Group 3	1.3417	1.3483	1.3554	1.3622	1.3688	1.3810
Group 4	1.3416	1.3483	1.3552	1.3620	1.3688	1.3811
Group 5	1.3416	1.3484	1.3550	1.3620	1.3687	1.3812

Fig. 12 **a** Transmission spectra of structures injected with 5%, 10%, 15%, 20%, and 25% aqueous solutions of vitamin C. **b** Variation of refractive index with concentration after linear fitting

Conclusion

In this study, we suggest a MIM waveguide structure based on the transmission properties of SPPs. The following findings are also reached:

(1) We design a new structure of a MIM main waveguide coupled with a copper coin-type ring cavity and a double semi-elliptical ring cavity based on SPPs. The structure can excite double Fano resonance.

(2) We use the finite element method to analyze the effect of the structural parameters of this structure on the sensing performance. Then, we optimize the structure for the sensing performance. After optimization, compared to existing similar sensing structures, our study achieves relatively high sensitivity and FOM. The sensitivity of the structure can reach 1150.00 nm/RIU, and the FOM value is 115.

(3) We inject an aqueous solution of vitamin C into the present structure. As the concentration of the vitamin C aqueous solution changes, its refractive index changes. The change in refractive index in turn causes the wavelength of the Fano resonance to change. Therefore, the structure can be used to measure the concentration of vitamin C aqueous solution.

Compared with other sensors of the same type, our proposed novel MIM waveguide structure has higher sensitivity and FOM. The design of this structure provides a reliable new method for the concentration measurement of vitamin C aqueous solution. This study has important implications for the development of highly integrated medical optical sensors.

Declarations

Conflict of Interest The authors declare no competing interests.

References

1. Barnes WL, Dereux A, Ebbesen TW (2003) Surface plasmon subwavelength optics. Nature 424(6950):824–830

2. Xiaoyu Z, Fengxiang W, Ying G, Wenjuan W, Luo Yongfeng Wu, Wen HJ, Ziqing J, Ziqiang P, Genghua H, Rong S (2023) Research on linear array scanning lidar and photon signal processing technology based on InGaAs single-photon detector[J]. Infrared and Laser Engineering 52(3):20220474

3. Miroshnichenko AE, Flach S, Kivshar YS (2010) Fano resonances in nanoscale structures. Rev Mod Phys 82(3):2257

4. Butt MA, Kazanskiy NL, Khonina SN (2020) Highly integrated plasmonic sensor design for the simultaneous detection of multiple analytes. Curr Appl Phys 20(11):1274–1280

5. Zhu J, Li N (2020) MIM waveguide structure consisting of a semicircular resonant cavity coupled with a key-shaped resonant cavity. Opt Express 28(14):19978–19987

6. Zhang Z, Wang J, Zhao Y (2011) Numerical investigation of a branch-shaped filter based on metal-insulator-metal waveguide. Plasmonics 6:773–778

7. Zheng Y, Yi Z, Liu Li, Xianwen Wu, Liu H, Li G, Zeng L, Li H, Pinghui Wu (2023) Numerical simulation of efficient solar absorbers and thermal emitters based on multilayer nanodisk arrays. Appl Therm Eng 230:120841

8. Fuyan Wu, Shi P, Yi Z, Li H, Yi Y (2023) Ultra-broadband solar absorber and high-efficiency thermal emitter from UV to mid-infrared spectrum. Micromachines 14(5):985

9. Lai R, Shi P, Yi Z, Li H, Yi Y (2023) Triple-band surface plasmon resonance metamaterial absorber based on open-ended prohibited sign type monolayer graphene. Micromachines 14(5):953

10. Zhao X, Zhang Z, Yan S (2017) Tunable Fano resonance in asymmetric MIM waveguide structure. Sensors 17(7):1494

11. Yang Q, Liu X, Guo F (2020) Multiple Fano resonance in MIM waveguide system with cross-shaped cavity. Optik 220:165163

12. Tang Y, Zhang Z, Wang R (2017) Refractive index sensor based on Fano resonances in metal-insulator-metal waveguides coupled with resonators. Sensors 17(4):784

13. Haslinger MJ, Sivun D, Pöhl H (2020) Plasmon-assisted direction- and polarization-sensitive organic thin-film detector. Nanomaterials 10(9):1866

14. Zhu J, Jin G (2021) Detecting the temperature of ethanol based on Fano resonance spectra obtained using a metal-insulator-metal waveguide with SiO 2 branches. Opt Mater Express 11(9):2787–2799

15. Rahmani Z, Rezaee N (2019) The reflection and absorption characteristics of one-dimensional ternary plasma photonic crystals irradiated by TE and TM waves. Optik 184:134–141

16. Yan J, Liu P, Lin Z (2015) Directional Fano resonance in a silicon nanosphere dimer. ACS Nano 9(3):2968–2980

17. Fano U (1961) Effects of configuration interaction on intensities and phase shifts. Phys Rev 124(6):1866

18. Chen L, Liu Y, Yu Z (2016) Numerical analysis of a near-infrared plasmonic refractive index sensor with high figure of merit based on a fillet cavity. Opt Express 24(9):9975–9983

19. Wu T, Liu Y, Yu Z (2014) The sensing characteristics of plasmonic waveguide with a ring resonator. Opt Express 22(7):7669–7677

20. Zhu J, Jin G (2022) Performance enhancement of solar cells based on high photoelectric conversion efficiency of h-BN and metal nanoparticles. Opt Express 30(8):13469–13480

21. Pang S, Huo Y, Xie Y (2016) Fano resonance in MIM waveguide structure with oblique rectangular cavity and its application in sensor. Opt Commun 381:409–413

22. Kim KY, Cho YK, Tae HS (2006) Light transmission along dispersive plasmonic gap and its subwavelength guidance characteristics. Opt Express 4(1):320–330

23. Chen J, Sun C, Gong Q (2014) Fano resonances in a single defect nanocavity coupled with a plasmonic waveguide. Opt Lett 39(1):52–55

24. Xie C (2021) Refractive index sensing based on multiple Fano resonances in a split-ring cavity-coupled MIM waveguide. Photonics 8(11):472

25. Li P, Liu J, Huang P (2020) Tunable fiber-tip lens based on thermo-optic effect of amorphous silicon. Chin Opt Lett 18(3):030602

26. Montesinos-Ballester M, Liu Q, Vakarin V (2019) On-chip Fourier-transform spectrometer based on spatial heterodyning tuned by thermo-optic effect. Sci Rep 9(1):14633

27. Bekshaev AY, Angelsky OV, Zheng J (2021) Microscopic analysis of the energy, momentum, and spin distributions in a surface plasmon-polariton wave. Opt Mater Express 11(7):2165–2191

28. Sannomiya T, Konecna A, Matsukata T (2019) Cathodoluminescence phase extraction of the coupling between nanoparticles and surface plasmon polaritons. Nano Lett 20(1):592–598

29. Zhu J, Wang G (2019) Sense high refractive index sensitivity with Bragg grating and MIM nanocavity. Results Phys 15:102763

30. Nehl CL, Liao H, Hafner JH (2006) Optical properties of star-shaped gold nanoparticles. Nano Lett 6(4):683–688

31. Xiao G, Xu Y, Yang H (2021) High sensitivity plasmonic sensor based on Fano resonance with inverted U-shaped resonator. Sensors 21(4):1164

32. Wang Q, Ouyang Z, Sun Y (2018) Tunable nanosensor based on Fano resonances created by changing the deviation angle of the metal core in a plasmonic cavity. Sensors 18(4):1026

33. Liwen S, Chonglin G, Qiantao C, Lin H, Zhongan Z, Longfei L, Shan Q, Aiguo Z, Wei Y, Hui J, Zhihui Z, Jiaqing L, Zhenxu B, Zhiming L (2023) Wide-range external-cavity tunable semiconductor laser with mode-hopping free[J]. Infrared Laser Eng 52(8):20230374

34. El Haffar R, Farkhsi A, Mahboub O (2020) Optical properties of MIM plasmonic waveguide with an elliptical cavity resonator. Appl Phys A 126:1–10

35. Zhu J, Yin J (2022) Optical method for detecting the concentration of sucrose based on plasmonic nanostructures. Carbon Lett 1–9

36. Xu Q, Zhu J (2022) Glycerol concentration sensor based on the MIM waveguide structure. Frontiers in Physics 10:1089

37. Ledford H (2014) Vitamin C injections ease ovarian-cancer treatments. Nature 14637

38. Kim K, Bae ON, Koh SH (2015) High-dose vitamin C injection to cancer patients may promote thrombosis through procoagulant activation of erythrocytes. Toxicol Sci 147(2):350–359

39. Lukosz W, Pliska P (1991) Determination of thickness and refractive index of SiO2 films on silicon wafers using an Abbe refractometer. Opt Commun 85(5–6):381–384

40. García-Valenzuela A, Contreras-Tello H, Márquez-Islas R (2013) Rigorous modelling of light's intensity angular-profile in Abbe refractometers with absorbing homogeneous fluids. J Phys Conf Ser. IOP Publishing 450(1):012022